

Research Article

Controllable Synthesis and Photocatalytic Activity of Nano-BiOBr Photocatalyst

Xiaoyang Wang, Fuchun Zhang , Yanning Yang, Yu Zhang, Lili Liu, and Wenli Lei

College of Physics & Electronic Information, Shaanxi Key Laboratory of Intelligent Processing of Big Energy Data, Yan'an University, Yan'an, 716000 Shanxi, China

Correspondence should be addressed to Fuchun Zhang; zhangfuchun72@163.com

Received 19 November 2019; Accepted 22 January 2020; Published 24 February 2020

Guest Editor: Domenico Lombardo

Copyright © 2020 Xiaoyang Wang et al. This is an open access article distributed under the Creative Commons Attribution License, which permits unrestricted use, distribution, and reproduction in any medium, provided the original work is properly cited.

Nano-BiOBr photocatalysts were successfully prepared by hydrothermal synthesis using the ethylene glycol solution. The nano-BiOBr photocatalysts were characterized and investigated by X-ray diffractometry (XRD), scanning electron microscopy (SEM), photoluminescence (PL), and UV-vis diffuse reflectance spectroscopy (UV-Vis DRS), and the catalytic ability toward photodegradation of rhodamine B (RhB) was also explored. The results showed that the crystallinity of the nano-BiOBr photocatalyst decreased with the increase of the concentration, while it increased with the amount of the applied deionized water. The morphology of the nano-BiOBr photocatalyst changed from microspheres to cubes and then to a mixture of microspheres and flakes with the increasing of the concentration and from microspheres to flakes with the addition of the deionized water. The results indicated that the concentration and solvents have an essential influence on the bandgap energy values of the nano-BiOBr photocatalyst, and photocatalyst showed an excellent photocatalyst activity toward photodegradation of RhB. The degradation yields of photocatalyst decreased with the increase of the concentration and increased with the addition of the deionized water. PL intensity of photocatalyst increased with the increase of the concentration and weakened with the addition of the deionized water.

1. Introduction

In recent years, the phenomenon of global water pollution has become a more and more severe issue with the rapid development of the economy, which has attracted widespread attention because of the close relationship between water resources and people's daily work and life [1, 2]. Many ways can cause water pollution, one of them being the textile industry and wastewaters with organic dye, which are challenging due to their poor biodegradability [3–5]. Semiconductor bismuth halide (BiOX, X = Cl, Br, I)-based photocatalysts have attracted extensive attention from researchers because of their unique structure and excellent photocatalytic properties [6, 7]. BiOBr was the target material of the presented investigations because of its moderate bandgap, open layered structure, high oxidation ability, indirect transition mode, high visible light response ability, and excellent stability [8, 9]. There are many methods to

prepare BiOBr, such as high temperature-based solid-state [10], hydrothermal [11], solvothermal [12], water- (alcohol-) based [13], ultrasound-assisted [14], and electrospinning method [15]. Among them, hydro- and solvothermal methods are the most commonly used synthesis pathways. The structure, morphology, crystallinity, and phase formation of the photocatalysts can be effectively obtained through controllable synthesis because of the slow product formation rate, simple and easy ways to control reaction conditions, and stable reaction environment during the water- (solvent-) based thermal reaction [16]. For example, nano-BiOBr microspheres were synthesized previously by the solvothermal method using ethylene glycol (EG) as a solvent [17]. On the other hand, nano-BiOX microspheres were obtained using other solvothermal methods and the same solvent EG [18]. BiOBr/SrFe₁₂O₁₉ nanosheets were synthesized by the solvothermal method using deionized water (DI) as a solvent [19]. AgBr/BiOBr nano-heterostructure-decorated

polyacrylonitrile nanofibers were synthesized by electrospinning technique and solvothermal treatment in the presence of an EG solution as the reductant [20].

Therefore, the present paper is aimed at using $\text{Bi}(\text{NO}_3)_3 \cdot 5\text{H}_2\text{O}$ and CTAB as raw materials, with EG and DI as a solvent, under the condition of different concentrations and different solvents to obtain nano-BiOBr photocatalyst. The influences of different solvents and concentrations of precursors on the structure, morphology, optical properties, and photocatalytic activities were also investigated systematically.

2. Experiment Section

2.1. Synthesis of Nano-BiOBr Photocatalyst. In the first step, 2 mmol of $\text{Bi}(\text{NO}_3)_3 \cdot 5\text{H}_2\text{O}$ is added to 80 ml of EG, and the solution was ultrasonicated until it was completely dissolved (obtaining solution A). Afterward, 2 mmol of CTAB was introduced into solution A, stirred magnetically until it was completely dissolved (solution B). Next, solution B was introduced into a high-temperature reactor (the filling degree is 80%), and after constant temperature reaction at 180°C for 10 hours in an incubator, the solution was naturally cooled to room temperature, and the precipitate was separated. Finally, the precipitate was washed with DI and alcohol, and then, the nano-BiOBr photocatalyst was finally obtained after the drying procedure at 80°C for 12 hours. Table 1 shows the abbreviation and synthesis parameters of nano-BiOBr photocatalyst obtained with different synthesis conditions, abbreviating them with (a)–(d) in the latter stages of the manuscript.

2.2. Characterization of Nano-BiOBr Photocatalyst. The crystalline phases were determined by a Bruker D8 Advance X-ray diffractometer (XRD) using a $\text{Cu K}\alpha$ ($\lambda = 0.15418 \text{ nm}$) radiation in the $\theta \sim 2\theta$ Bragg. The morphologies of the as-prepared samples were observed and investigated by a field emission scanning electron microscope (FESEM, Nova NanoSEM 450, FEI). The UV-vis absorption spectra of the samples were measured with a Cary 5000 (Agilent, USA). The photoluminescence (PL) spectra were observed with a He-Cd laser 280 nm.

2.3. Determination of the Photocatalytic Activity of the Nano-BiOBr Photocatalyst. The photocatalytic reactions were carried out in a CEL-LAB500E4 multisite photochemical reaction system. The catalytic activity of the target degradation product was evaluated by using nano-BiOBr photocatalyst under the visible light source. In a typical photocatalytic experiment, 0.05 g of the nano-BiOBr photocatalyst was dispersed into 50 ml of RhB (10 mg/l) solution and magnetically stirred in the dark for 30 min to reach the adsorption-desorption equilibrium between RhB and the nano-BiOBr photocatalyst. Then, the light source was turned on, and a sample of 4 ml of the suspension was continually taken from the reaction cell at every 15 minutes and centrifuged. Finally, the absorbance of the supernatant at the maximum absorption wavelength was analysed through an ultraviolet-visible spectrophotometer (UV-1901). The degra-

TABLE 1: The specific process parameters of samples.

Sample	$V_1 : V_2$	$C_{\text{Bi}} : C_{\text{Br}}$	T (°C)	Notes
(a)	8 : 0	1 : 1	180	V_1 : EG volume
(b)	8 : 0	1 : 3	180	V_2 : DI volume
(c)	8 : 1	1 : 3	180	C_{Bi} : the source of Bi^{+3}
(d)	8 : 0	1 : 5	180	C_{Br} : the source of Br^-

ation efficiencies were calculated according to the expression of degradation rate $(1 - A/A_0)$, where A_0 is the absorbance of the target degradation at its maximum absorption wavelength before illumination, and A is the absorbance value after illumination for a certain time.

3. Results and Discussion

3.1. XRD Analysis. The XRD patterns of nano-BiOBr photocatalyst at different concentrations and different solvents are shown in Figure 1. It is clear that the prepared nano-BiOBr photocatalysts were consistent with the standard diffraction pattern of tetragonal BiOBr (PDF#85-0862) (Figure 1(a)). No other specific diffraction peaks were detected, indicating that the nano-BiOBr photocatalysts prepared in different concentrations and different solvents are pure tetragonal nanoparticles. The intensity of the diffraction peak is weakened with the increase of the concentration, indicating that the concentrations are the key factor affecting the crystallinity of nano-BiOBr photocatalyst, 2-theta was right-shifted, and the crystal space d decreased according to the Prague equation ($d \sin \theta = n\lambda$). The intensity of the diffraction peak increases with the increase of DI, indicating that the increase of DI throughout all the experiments is beneficial to increase the crystallinity of nano-BiOBr photocatalyst; the influence factors were more, and the main reason remains to be further studied.

In order to study the stability of the nano-BiOBr photocatalyst, the XRD of the nano-BiOBr photocatalyst after the photocatalytic reaction was investigated (Figure 1(b)). Compared with the results before the photodegradation, there are no noticeable changes in the crystal phases of the samples.

3.2. SEM Analysis. Figure 2 shows the SEM images of nano-BiOBr photocatalysts prepared using different concentrations and different solvents. As shown in Figure 2(a), BiOBr microspheres with a diameter of $\sim 2 \mu\text{m}$ were obtained, and the BiOBr microspheres are self-assembled from irregular nanosheets with a thickness of $\sim 10 \text{ nm}$. From Figure 2(b), BiOBr cubes of $\sim 2 \mu\text{m}$ are obtained, BiOBr being also self-assembled from irregular nanosheets in a fixed manner. Compared with (a) photocatalyst, (b) photocatalyst is self-assembled from nanosheets more densely, and the thickness of the nanosheets is higher ($\sim 20 \text{ nm}$). As shown in Figure 2(c), irregular sheetlike nano-BiOBr was obtained; compared with (b) photocatalyst, (c) photocatalyst is a nanosheet with a thickness of $\sim 15 \text{ nm}$. From Figure 2(d), it can be observed that a mixture of BiOBr microspheres and sheetlike BiOBr is obtained. BiOBr microspheres are tightly assembled from irregular nanosheets with a thickness of $\sim 15 \text{ nm}$.

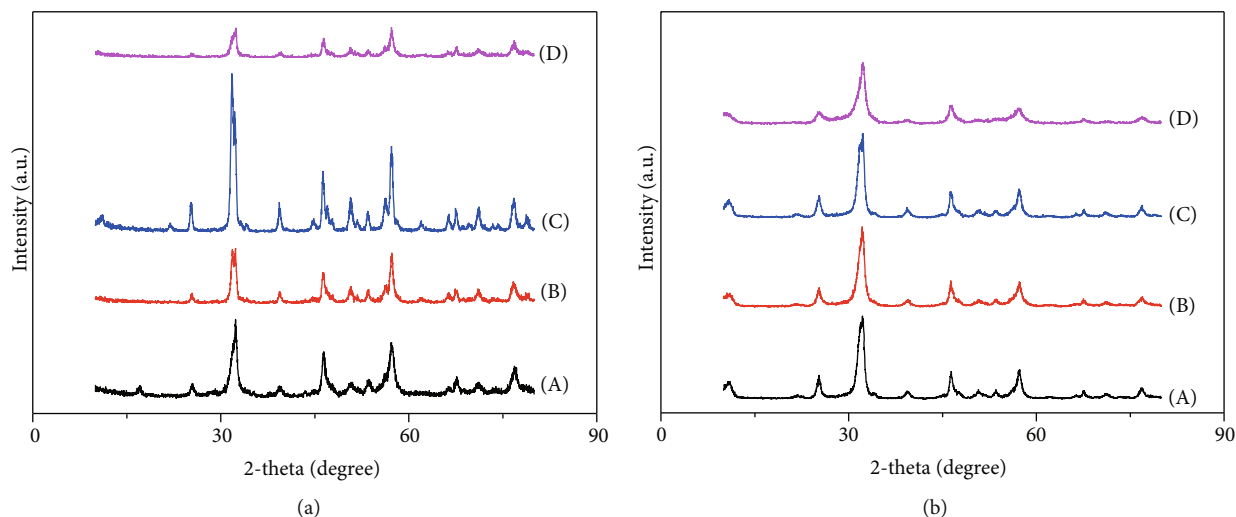


FIGURE 1: XRD patterns of samples (a) before and (b) after the reaction.

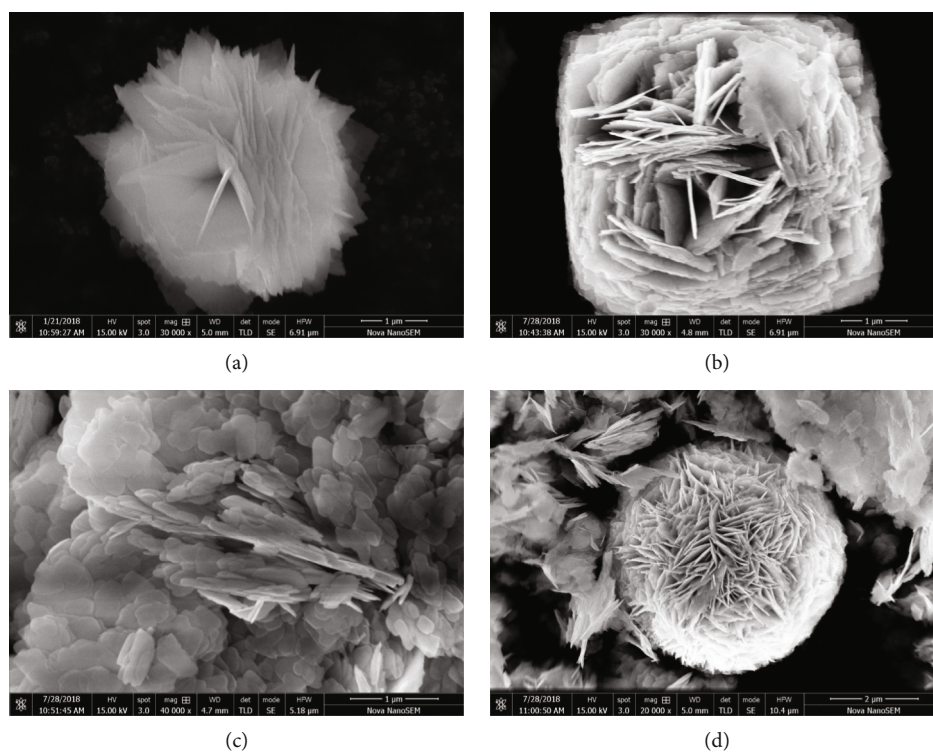


FIGURE 2: SEM images of (a)–(d) photocatalysts.

Compared with (b) photocatalysts, (d) photocatalysts have more unassembled nanosheets, and the thickness of the nanosheets is smaller and assembled in a way that cubes become microspheres. The results showed that the morphology of the nano-BiOBr photocatalyst changed from microspheres to cubes and then to a mixture of microsphere and flakes with the increasing of the concentration of precursors. Moreover, the morphology of nano-BiOBr photocatalyst changed from microspheres to flakes with the addition of DI.

3.3. UV-Vis DRS Analysis. Figure 3 shows the UV-vis diffuse reflectance spectra and corresponding bandgap energies of the nano-BiOBr photocatalyst. It can be observed that the absorption edges of (a)–(d) photocatalysts can be found at 439, 450, 446, and 453 nm, respectively, indicating that the absorption wavelength range of (d) photocatalyst is the largest, and the absorption wavelength range of (a) photocatalyst is the smallest, meaning that, more visible light can be absorbed with the increasing of the concentration; the absorbed visible light is reduced with the addition of DI.

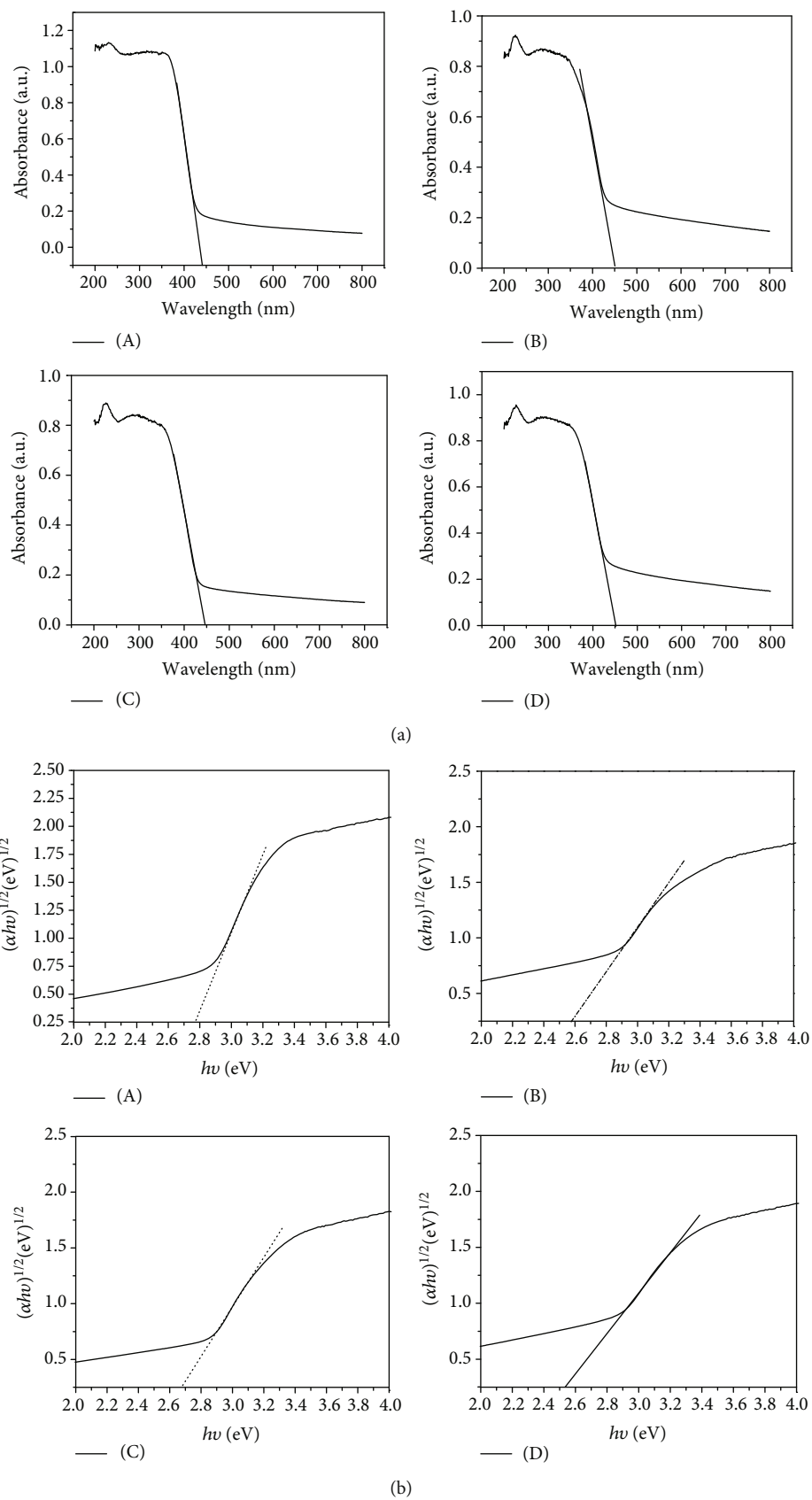


FIGURE 3: UV-vis diffuse reflectance spectra and a corresponding bandgap width of (A)–(D) photocatalysts.

The position of the absorption edge is closely related to the forbidden bands of the semiconductor photocatalyst. The forbidden bandwidth of the BiOBr photocatalyst is calculated by Equation (1) [21].

$$\alpha h\nu = A(h\nu - E_g)^{n/2}, \quad (1)$$

where α , h , ν , A , and E_g represent the intrinsic absorption coefficient, the Planck constant, the frequency of light, the proportion constant of photocatalyst, and the bandgap width of semiconductor, respectively. $n = 2$ for direct bandgap semiconductor, and $n = 4$ for indirect bandgap semiconductor. $n = 4$ because BiOBr photocatalyst is an indirect bandgap semiconductor. Using the formula on the $h\nu \sim (\alpha h\nu)^{1/2}$ curve, as shown in Figure 3(b), it can be observed that the tangent in the middle section of the curve and the intercept between tangent and abscissa is the bandgap of BiOBr photocatalyst. The bandgap of (a)–(d) photocatalyst measured by plotting and tangent fitting was 2.77 eV, 2.57 eV, 2.67 eV, and 2.53 eV, respectively. It can be observed that the bandgap decreases continuously with the increase of the concentration and the bandgap increases with the addition of DI. It can be concluded that the concentration of substances and solvents has an important influence on the bandgap energy values of BiOBr photocatalyst.

3.4. Photodegradation of RhB Using Nano-BiOBr Semiconductors

3.4.1. UV-Vis Absorption Spectral Analysis. Figure 4 shows the UV-vis absorption spectral changes of RhB aqueous solution vs. irradiation time in the presence of the (a)–(d) photocatalysts. With the increase of the irradiation time, the absorption maximum of the spectra declined, and the band shifted to a smaller wavelength, which indicates N-demethylation and the destruction of the conjugated structure in the RhB photodegradation process [22]. The blue-shifted band implies that the main photocatalytic degradation path of the RhB is N-demethylation. The major peaks are reduced gradually during visible light irradiation, indicating a step-by-step degradation of RhB. The RhB UV-vis absorption spectra of the (a) photocatalyst were approximately a straight line after 60 min of illumination, indicating that the photocatalytic reaction of the (a) photocatalyst to RhB was mainly completed. The absorption peak of RhB in the visible light region of (a), (c), and (d) photocatalysts has completely disappeared after 80 min, and the decolourisation efficiency reaches 100%. The RhB solution photodegraded using (b) photocatalysts had a weak absorption peak at the end of the process. The findings are in accordance with the results obtained from previous sections, as the degradation efficiency of photocatalyst decreases with the increase of the concentration. On the other hand, the degradation efficiency of photocatalyst increased with the addition of DI.

3.4.2. Degradation Efficiency for RhB of BiOBr Photocatalysts. Figure 5 shows the degradation performance for RhB by photocatalysts prepared in different concentrations and different solvents. The results showed that the degradation per-

formance of photocatalyst declines in varying degrees with the increase of the concentration, which indicates that the concentration can change the degradation performance of the photocatalyst. The degradation performance of photocatalyst improves with the addition of DI. The degradation performance of (a)–(d) photocatalysts to RhB was 96.3%, 68.8%, 88.1%, and 81.3%, respectively, after 60 min of light irradiation. It can be summarised that (a) photocatalyst showed the highest photocatalytic activity for RhB.

3.5. PL Analysis. Nano-BiOBr photocatalyst using different concentrations and different solvents were characterized by photoluminescence (PL) spectroscopy to verify further the conclusions mentioned above. The excitation wavelength was 280 nm, and the emission range was 400 nm to 600 nm, as shown in Figure 6. The movement, transfer, and recombination rate of photogenerated electron-hole pairs were revealed by PL spectra. The lower the intensity of emission peaks in PL spectra, the higher the separation efficiency of electrons and holes in semiconductors and the higher the photocatalytic activity of photocatalysts that were observable [23]. It can also be seen that the PL intensity increases with the increase of the concentration, while the photocatalytic activity decreases. As can also be observed, the PL intensity is weakened with the addition of DI and the photocatalytic activity increased. It can be seen from the figure that all of the photocatalysts have emission peaks at 437 nm, 449 nm, and 466 nm and the order of luminous intensity is (b) > (d) > (c) > (a), which means that the recombination rate of electrons and holes of the four materials decreases gradually and the photodegradation performance is gradually enhanced, which is in accordance with the previous photocatalytic experiment results.

4. Conclusion

Nano-BiOBr photocatalysts were successfully prepared by the hydrothermal method. The influences of different concentrations and different solvents on structure, morphology, optical properties, and photocatalytic properties are investigated systematically. The results show that the crystallinity of the nano-BiOBr photocatalyst decreases with the increase of the concentration and increases with the increase of the DI. The morphology of the nano-BiOBr photocatalyst changes from microspheres to cubes and then to a mixture of microsphere and flakes with the increasing of concentration, from microspheres to flakes with the addition of DI. It was also proved that the concentration and solvents have an essential influence on the bandgap energy values of the nano-BiOBr photocatalyst. The degradation performance of photocatalyst with the decline in the increase of concentrations improves with the addition of DI. The semiconductor (a) showed the highest photocatalytic activity toward RhB. PL intensity of photocatalyst increased with the increase of the concentration and weakened by the addition of DI. Therefore, the high photocatalytic activity of photocatalysts for contaminant aqueous solution makes this research a new platform to develop flexible photocatalyst for practical applications in water purification.

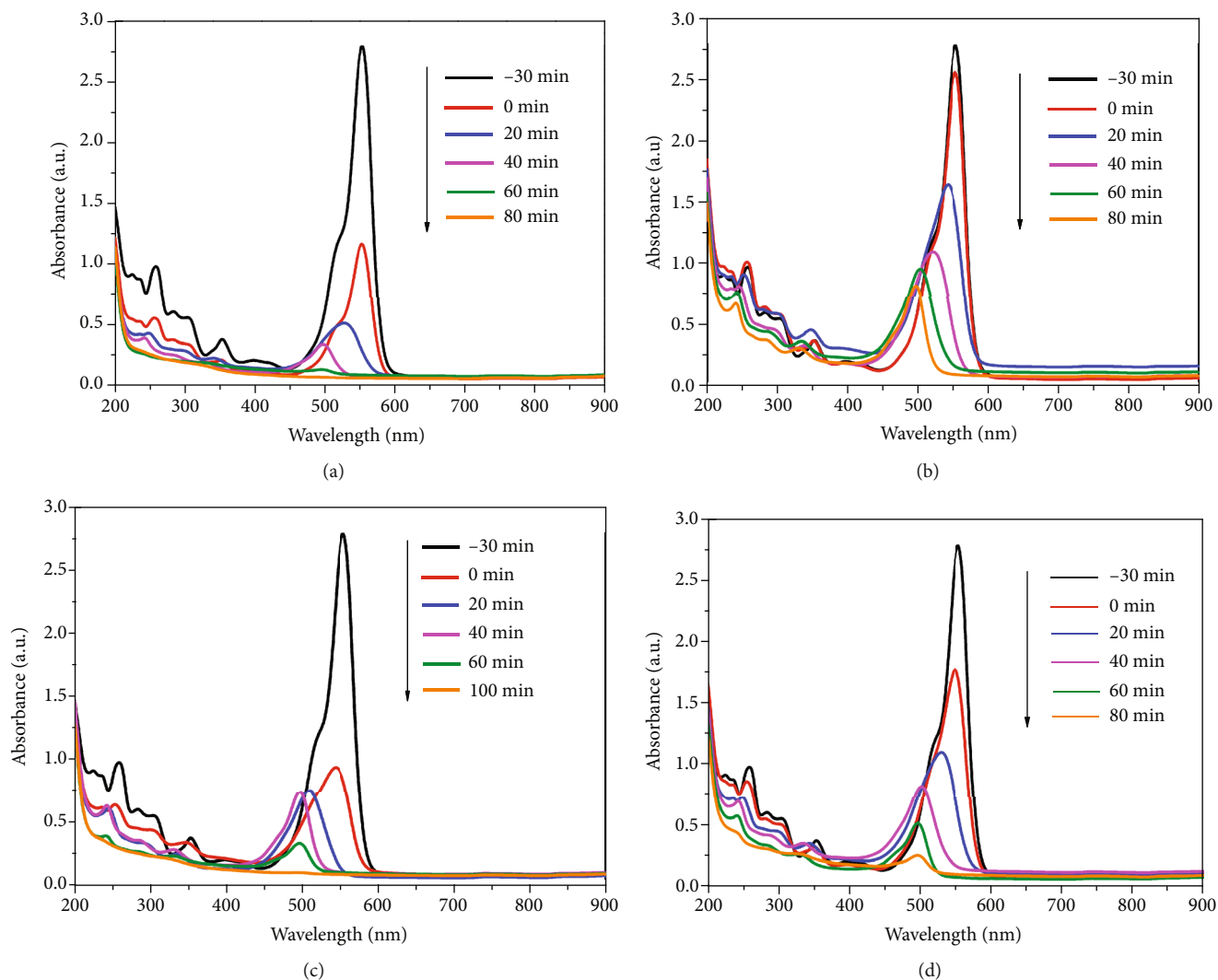


FIGURE 4: UV-vis absorption spectral changes of RhB aqueous solution as a function of irradiation time in the (a)–(d) photocatalysts.

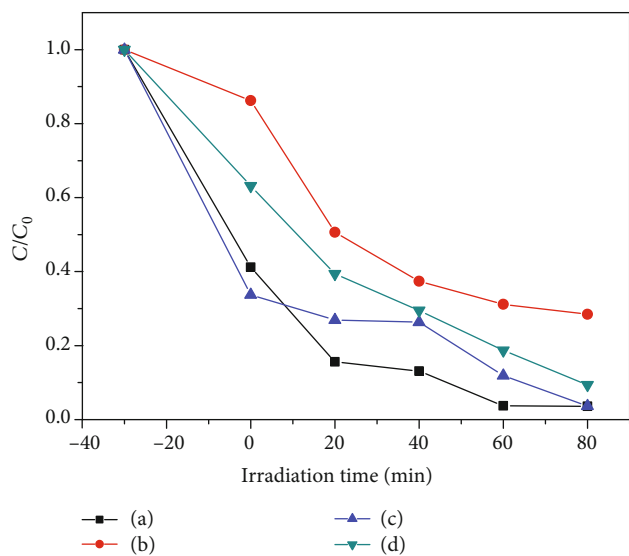


FIGURE 5: Degradation performance of (a)–(d) photocatalysts for RhB.

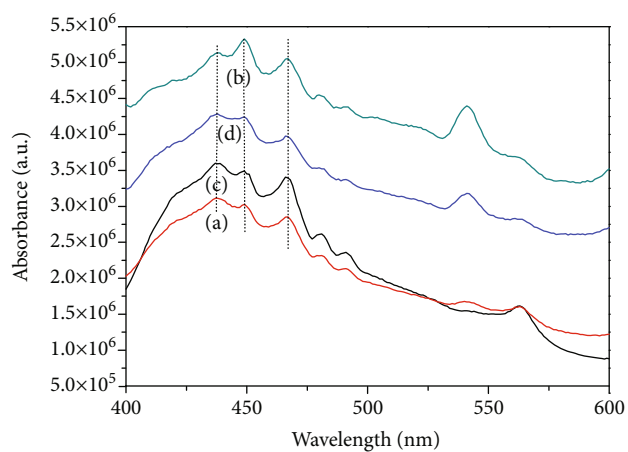


FIGURE 6: PL spectral of (a)–(d) photocatalysts.

Data Availability

The data used to support the findings of this study are available from the corresponding author upon request.

Conflicts of Interest

The authors declare that they have no conflicts of interest.

Acknowledgments

The project was supported by the National Natural Science Fund of China (61664008), the Scientific and Technological Innovation Team (2017CXTD-01), the Scientific Research Program Funded by Shaanxi Provincial Education Department (18JK0870), the Yan'an Science and Technology Research and Development Program (2018KG-01), the Yan'an University Ph.D. Research Project (YDBK2018-39), and the Yan'an University Industry-University-Research Cooperation Project (YDCXY2018-07).

References

- [1] P. A. Reddy, P. V. Reddy, E. Kwon, K. H. Kim, T. Akter, and S. Kalagara, "Recent advances in photocatalytic treatment of pollutants in aqueous media," *Environment International*, vol. 91, pp. 94–103, 2016.
- [2] W. Wang, G. Huang, J. C. Yu, and P. K. Wong, "Advances in photocatalytic disinfection of bacteria: development of photocatalysts and mechanisms," *Journal of Environmental Sciences*, vol. 34, no. 8, pp. 232–247, 2015.
- [3] C. G. Yu, G. Li, S. Kumar, K. Yang, and R. Jin, "Phase transformation synthesis of novel $\text{Ag}_2\text{O}/\text{Ag}_2\text{CO}_3$ heterostructures with high visible light efficiency in photocatalytic degradation of pollutants," *Advanced Materials*, vol. 26, no. 6, pp. 892–898, 2014.
- [4] Y. F. Yang, F. Zhou, S. Zhan, Y. Liu, and Y. Yin, "Enhanced photocatalytic activity of BiOCl hybridized with $g\text{-C}_3\text{N}_4$," *Journal of Inorganic and Organometallic Polymers and Materials*, vol. 26, no. 1, pp. 91–99, 2016.
- [5] Q. T. Yang, Q. L. Xie, N. C. Chen, and Y. J. Zhong, "Research progress on wastewater treatment by heavy metal ion imprinted polymer," *Materials Science Forum*, vol. 921, pp. 35–39, 2018.
- [6] A. Dandapat, H. Gnyayem, and Y. Sasson, "The fabrication of $\text{BiOCl}_x\text{Br}_{1-x}$ /alumina composite films with highly exposed {001} facets and their superior photocatalytic activities," *Chemical Communications*, vol. 52, no. 10, pp. 2161–2164, 2016.
- [7] Y. Huo, J. Zhang, M. Miao, and Y. Jin, "Solvothermal synthesis of flower-like BiOBr microspheres with highly visible-light photocatalytic performances," *Applied Catalysis B: Environmental*, vol. 111–112, pp. 334–341, 2012.
- [8] Y. Zhao, T. Yu, X. Tan, C. Xie, and S. Wang, "SDS-assisted solvothermal synthesis of rose-like BiOBr partially enclosed by {111} facets and enhanced visible-light photocatalytic activity," *Dalton Transactions*, vol. 44, no. 47, pp. 20475–20483, 2015.
- [9] Z. Fan, Y. Zhao, W. Zhai, L. Qiu, H. Li, and M. R. Hoffmann, "Facet-dependent performance of BiOBr for photocatalytic reduction of Cr(VI) ," *RSC Advances*, vol. 6, no. 3, pp. 2028–2031, 2016.
- [10] S. Perera, N. A. Zelenski, R. E. Pho, and E. G. Gillan, "Rapid and exothermic solid-state synthesis of metal oxyhalides and their solid solutions via energetic metathesis reactions," *Journal of Solid State Chemistry*, vol. 180, no. 10, pp. 2916–2925, 2008.
- [11] D. Zhang, M. Wen, B. Jiang, G. Li, and J. C. Yu, "Ionothermal synthesis of hierarchical BiOBr microspheres for water treatment," *Journal of Hazardous Materials*, vol. 211–212, no. 2, pp. 104–111, 2012.
- [12] X. Li, C. Dong, K. L. Wu et al., "Synthesis of nitrogen-doped graphene- BiOBr nanocomposites with enhanced visible light photocatalytic activity," *Materials Letters*, vol. 164, pp. 502–504, 2016.
- [13] K. Zhang, J. Liang, S. Wang et al., " BiOCl sub-microcrystals induced by citric acid and their high photocatalytic activities," *Crystal Growth & Design*, vol. 12, no. 2, pp. 793–803, 2012.
- [14] L. Kong, Z. Jiang, T. Xiao, L. Lu, M. O. Jones, and P. P. Edwards, "Exceptional visible-light-driven photocatalytic activity over $\text{BiOBr-ZnFe}_2\text{O}_4$ heterojunctions," *Chemical Communications*, vol. 47, no. 19, pp. 5512–5514, 2011.
- [15] H. Cheng, B. Huang, and Y. Dai, "Engineering BiOX ($X = \text{Cl, Br, I}$) nanostructures for highly efficient photocatalytic applications," *Nanoscale*, vol. 6, no. 4, pp. 2009–2026, 2013.
- [16] Z. Zhuang, Q. Peng, and Y. Li, "Controlled synthesis of semiconductor nanostructures in the liquid phase," *Chemical Society Reviews*, vol. 40, no. 11, pp. 5492–5513, 2011.
- [17] S. Hong, H. Ren, Y. Fang, Y. Huang, and R. Li, "Template-free solvothermal synthesis of flower-like BiOBr microspheres in ethanol medium for photocatalytic applications," *Russian Journal of Physical Chemistry A*, vol. 92, no. 5, pp. 984–991, 2018.
- [18] X. J. Wang, X. N. Xu, Y. J. Han, and X. N. Chen, "Highly efficient photocatalytic degradation of methyl orange and Rhodamine B by hierarchical BiOBr microspheres," *Crystal Research and Technology*, vol. 50, no. 5, pp. 405–412, 2015.
- [19] T. P. Xie, J. Hu, J. Yang et al., "Visible-light-driven photocatalytic activity of magnetic $\text{BiOBr}/\text{SrFe}_{12}\text{O}_{19}$ nanosheets," *Nanomaterials*, vol. 9, no. 5, p. 735, 2019.
- [20] M. Y. Zhang, Y. Qi, and Z. Y. Zhang, " AgBr/BiOBr nano-heterostructure-decorated polyacrylonitrile nanofibers: a recyclable high-performance photocatalyst for dye degradation under visible-light irradiation," *Polymers*, vol. 11, no. 10, p. 1718, 2019.
- [21] W. Gao, M. Wang, C. Ran et al., "One-pot synthesis of $\text{Ag}/\text{rGO}/\text{TiO}_2$ nanocomposites with high solar absorption and enhanced anti-recombination in photocatalytic applications," *Nanoscale*, vol. 6, no. 10, pp. 5498–5508, 2014.
- [22] S. Zhang and J. Yang, "Microwave-assisted synthesis of $\text{BiOCl}/\text{BiOBr}$ composites with improved visible-light photocatalytic activity," *Industrial & Engineering Chemistry Research*, vol. 54, no. 41, pp. 9913–9919, 2015.
- [23] Z. Wu, J. Liu, Q. Tian, and W. Wu, "Efficient visible light formaldehyde oxidation with 2D $p\text{-}n$ Heterostructure of $\text{BiOBr}/\text{BiPO}_4$ Nanosheets at room temperature," *ACS Sustainable Chemistry & Engineering*, vol. 5, no. 6, pp. 5008–5017, 2017.